"International Symposium on Cutting Edge of Computer Simulation of Solidification and Processes", Osaka, Japan, Nov. 14-16, 1999, pp. 113-128.

Detailed Simulation of Flow in Continuous Casting of Steel using K-ε, LES, and PIV

Brian G. Thomas, Hua Bai, Sivaraj Sivaramakrishnan, and S. Pratap Vanka

Department of Mechanical and Industrial Engineering
University of Illinois at Urbana Champaign
1206 West Green Street, Urbana IL 61801, U.S.A.
bgthomas@uiuc.edu

Abstract

During the continuous casting of steel, transient flow events can be very important to the generation of quality problems. These transient phenomena can be computationally modeled using Large Eddy Simulation (LES) models while conventional K-ε models yield time-averaged results. Recently, Particle Image Velocimetry (PIV) has been applied to measure quantitatively the transient velocity fields in water models of this process. Results using all three methods compare favorably and give new insight into the flow phenomena. The slide gate creates a strong swirl at the outlet ports of the nozzle, which is also predicted using a K-ε model. The inlet swirl is seen to persist more than halfway across the mold, causing a characteristic staircase velocity vector pattern in the PIV measurements when viewed in a plane parallel to the wide faces. Flow across the top surface was found in PIV to contain periods of 5-10s when the velocities were three to four times their mean values. This is likely related to inlet conditions and is important to the shear entrainment of the liquid flux at the top surface and level fluctuations. In both LES and PIV, the upper roll structure evolves chaotically between a single large recirculation structure and a set of distinct vortices. The lower rolls in PIV are significantly asymmetric for very long periods of time (~ 1-hour) and go through a repeating sequence of features. One of these features involves a short circuit between the upward and downward flow in the lower roll, which is also seen in the simulation. This appears to be inherent to the turbulent nature of the flow and is likely important to inclusion particle and bubble entrapment.

I. Introduction

Flow in the mold region during the continuous casting of steel is of great interest because it influences many important phenomena, which have far-reaching consequences on strand quality. These phenomena include the dissipation of superheat by the liquid jet impinging upon the solidifying shell (and temperature at the meniscus), the flow and entrainment of the top surface powder / flux layers, top-surface contour and level fluctuations, and the entrapment of subsurface inclusions and gas bubbles.

Flow in the mold can be studied using physical water models and mathematical models. The turbulent flow through the nozzle and in the mold of the continuous caster has been studied extensively using computational models based on the Reynolds Averaged Navier Stokes (RANS) approach [1-3]. The most popular of these are steady models using the k-ε turbulence model. Recently, computational models have been developed to simulate the detailed evolution of structures in the transient flow field. These include the Large Eddy Simulation method (LES). Scale water models have been applied with great success in previous work to study the flow of molten steel, owing to the similar kinematic viscosity of the two fluids, which governs much of the flow behavior. To better visualize and quantify the flow in these water models, Particle Image Velocimetry (PIV) has been applied recently to measure the transient velocity fields [4].

In this work, recent results using all three of these methods are compared and applied to yield new insights into transient flow phenomena in the continuous casting nozzle and mold. Comparisons are made of the time-averaged velocities, velocity fluctuations and transient flow features in all parts of the mold. The comparisons investigate the validity of the simplifying assumptions made in developing the models. This work is part of an ongoing effort to develop mathematical models of the continuous casting process and to apply them to increase understanding and solve problems of practical interest.

II. Description of Water Model, PIV, and Simulation Domains

The flow from the tundish passes through a slide gate, which moves at right angles to the wide face to restrict the opening in the nozzle and thereby control the flow rate. Figure 1 shows the outline of the slide-gate nozzle. The flow then enters the mold cavity and flows out the bottom, through three pipes attached to circular 35mm diameter outlets in the bottom plate. Figure 2 shows a sketch of the experimental mold model and the corresponding computational domain. The experimental domain is nominally symmetric with respect to the centerline shown in the figure. Tables I and II list the main dimensions and casting conditions for the nozzle and mold models respectively. The mold does not have a constant thickness but tapers from top to bottom, thus simulating only the liquid portion of the steel caster.

Flow visualization and velocity measurements were made using 0.4-scale Plexiglas water models of the tundish, nozzle and mold of the caster at LTV Steel (Cleveland, OH) [5]. Sequences of instantaneous velocity measurements were obtained using the PIV (Particle Image Velocimetry) system of DANTEC Measurement Technology. The positions of tracer particles are recorded digitally when illuminated by two consecutive pulses of sheets of laser light. Knowing the time interval between pulses (1.5 x 10^{-3}s), and the distances moved by the particles (from image processing), a complete instantaneous velocity field is obtained. This procedure is usually repeated every 0.2s and the results from at least 50 such exposures were averaged to obtain the time-averaged velocity field. In order to get good resolution in the PIV measurements, the domain was divided into four regions: the vicinity near the nozzle ports, the top region of the mold containing the jet and the upper roll, the middle region containing both the lower rolls and the bottom region containing part of the lower roll. Further details on the PIV measurement system are provided elsewhere [6].

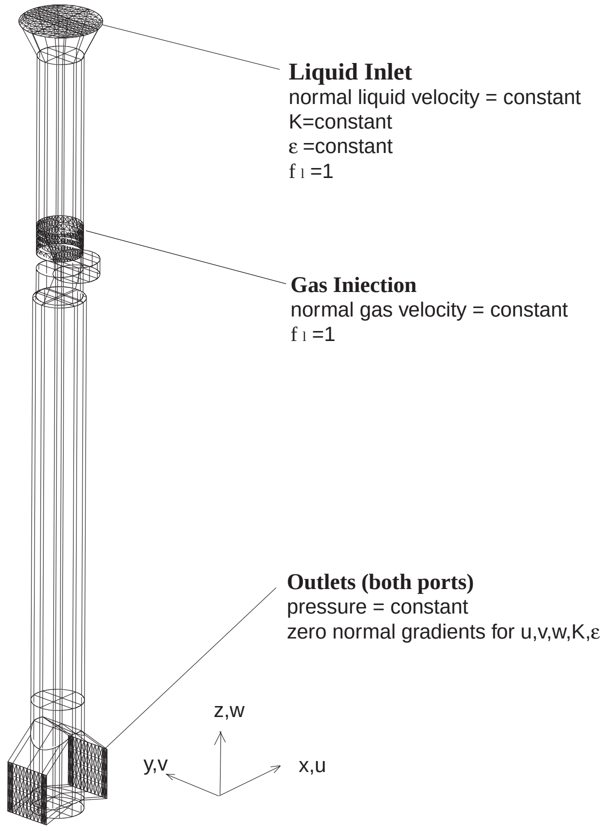

Figure 1 – Nozzle domain and boundary conditions

Table I – Nozzle Model Conditions (0.4 scale)

Dimension / Condition	Value
Bore (SEN) diameter	32 mm
Port width x height	31mm x 32mm
Port thickness	11 mm
Port angle, lower edge	15˚ down
Port angle, upper edge	40˚ down
Bottom well recess depth	4.8 mm
UTN diameter	28 mm
Slide-gate diameter	28 mm
Slide-gate thickness	18 mm
Liquid flow rate at inlet	7.07 x10^{-4} m^3/s
Nozzle length (total)	510 mm
Tundish bath depth	400~410 mm
Slide-gate orientation	90°
SEN submergence depth	80 mm
Slide-gate opening (FL)	52%
Liquid kinematic viscosity	1.0 x10^{-6} m^2/s
Gas volume fraction	5.8%
Gas density	1.29 kg/m^3
Gas molecular viscosity	1.54x10^{-5} kg/m-s
Gas bubble diameter	1 mm

III. Numerical Models

The mathematical models in this work satisfy mass and momentum conservation in the computational domain by solving the continuity equation and the conservative form of the Navier Stokes equations for isothermal incompressible Newtonian fluids,

$$\frac{\partial v_j}{\partial x_j} = 0 \tag{1}$$

$$\frac{\partial}{\partial t}\rho v_i + \frac{\partial}{\partial x_j}\rho v_j v_i = -\frac{\partial P}{\partial x_i} + \frac{\partial}{\partial x_j}\mu_{eff}\left(\frac{\partial v_j}{\partial x_i} + \frac{\partial v_i}{\partial x_j}\right) \tag{2-4}$$

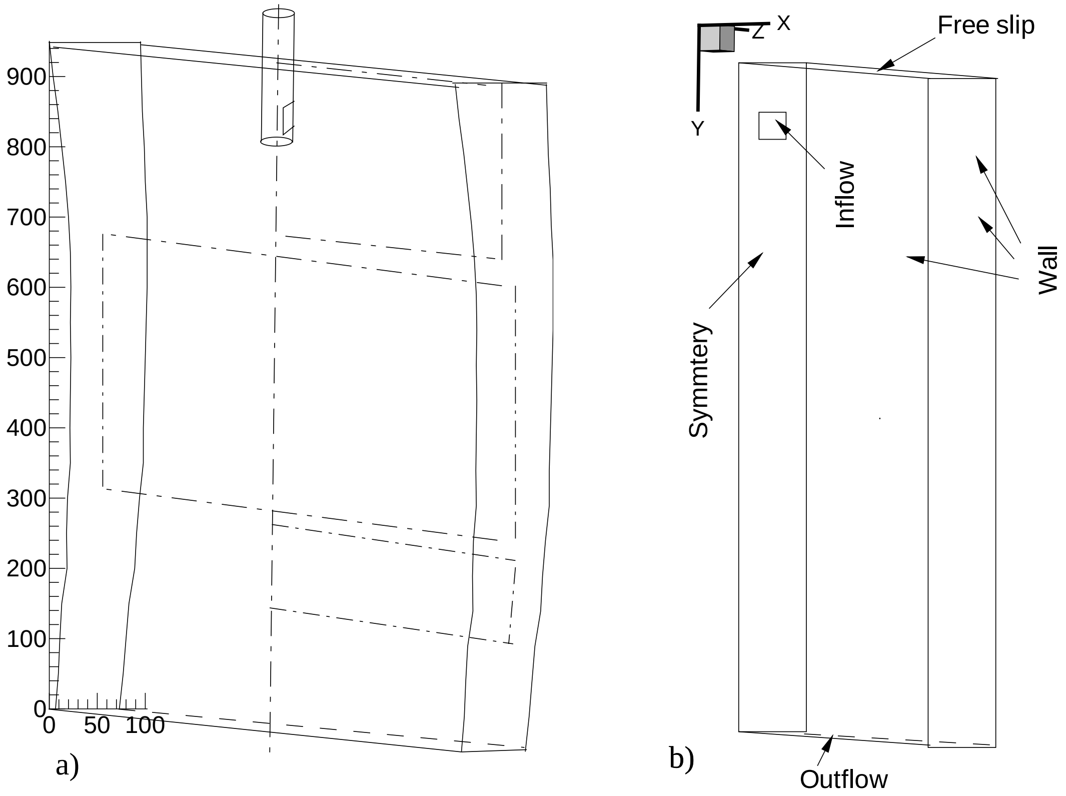

Figure 2: Scale drawing of (a) water model and (b) simulation domains. The water model domain also shows the three rectangular regions in which PIV data were collected.

Table II Mold Water Model and Simulation Conditions

Dimension / Condition	**Water Model**	**Simulation**
Length of the model	950 mm	956 mm
Thickness of model	95 mm (top) to 65 mm (bottom)	80 mm (constant)
Port opening	31 x 31 mm	31 x 31 mm
Top surface	Free surface	Free slip boundary
Flow rate through each port	3.528×10^{-4} m^3/s (5.6 gal/min)	3.528×10^{-4} m^3/s (5.6 gal/min)
Average inlet velocity	424 mm/s	424 mm/s
Average jet inlet angle	30^o	30^o
SEN Submergence depth (top of port to top surface)	75 ± 3mm	72 mm
Outlets at bottom	1.5 round 35mm diameter outlets along each half	1.5 square 35mm outlets
Kinematic viscosity (water)	1×10^{-6} m^2/s	1×10^{-6} m^2/s
Gas flow rate (cubic ft / hr)	0.0	0.0

where $\partial/\partial t$ = differentiation with respect to time (s^{-1})
ρ = density (kg/m^3)
v_i = velocity component in x_i direction (m/s)
x_i = coordinate direction, x,y, or z (m)
P = pressure field (N/m^2)
μ_{eff} = effective viscosity (kg/m-s)
i = index referring to equation in the x, y, or z directions
j = index which, when repeated in a term, implies summation over all coord. direcs.

The solution yields the pressure and velocity components at every point in the three-dimensional domain. At the high flow rates involved, these models must account for turbulence.

Large Eddy Simulation Model

The simplest and most accurate way to model turbulence is to use a fine enough grid (mesh) to capture all of the turbulent eddies and their motion with time. This method, known as "direct numerical simulation", is computationally very demanding. The present work employs a faster method called "large eddy simulation" or LES, which uses a less refined grid to capture only the large scale eddies. For high velocities, a turbulence model is often used at the sub-grid scale in order to diffuse the kinetic energy of these scales, although this was not needed in the present work.

The equations in the LES model are discretized using the Harlow-Welch fractional step procedure [7] on a staggered grid. Second order central differencing is used for the convection terms and Crank Nicolson scheme [7] is used for the diffusion terms. The Adams-Bashforth scheme [7] is used to discretize in time with second order accuracy. The implicit diffusion terms are solved for using Alternate Line Inversion. The Pressure Poisson equation is solved using a direct Fast Fourier Transform solver. For parallelization, 1-D domain decomposition with MPI (Message Passing Interface) is used. To simulate the mold in Figure 2b), a rectangular computational grid of 1.5 million nodes (128, 184, and 64 points along the X, Y and Z axes respectively) was employed and the time step is 0.001s. The LES simulations are quite slow and take 18 CPU s per time step or 13 days (total CPU time) on an Origin 2000 for 60s of flow simulation.

CFX Model

For improve computationally efficiency, turbulence was also modeled on a courser grid using the K - ε model, which averages the effect of turbulence using an increased effective viscosity field, μ_{eff}.

$$\mu_{eff} = \mu_0 + \mu_t = \mu_0 + \rho C_\mu \frac{K^2}{\varepsilon} \tag{5}$$

where μ_o, μ_t = laminar and turbulent viscosity fields (kg/m-s)
ρ = fluid density (kg/m^3)
C_μ = empirical constant = 0.09
K = turbulent kinetic energy field, m^2/s^2
ε = turbulent dissipation field, m^2/s^3

This approach requires solving two additional partial differential equations for the transport of turbulent kinetic energy and its dissipation:

$$\rho \frac{\partial (v_j K)}{\partial x_j} = \frac{\partial}{\partial x_j}\left(\frac{\mu_t}{\sigma_K}\frac{\partial K}{\partial x_j}\right) + \mu_t \frac{\partial v_j}{\partial x_i}\left(\frac{\partial v_i}{\partial x_j} + \frac{\partial v_j}{\partial x_i}\right) - \rho\varepsilon \qquad (6)$$

$$\rho \frac{\partial (v_j \varepsilon)}{\partial x_j} = \frac{\partial}{\partial x_j}\left(\frac{\mu_t}{\sigma_\varepsilon}\frac{\partial \varepsilon}{\partial x_j}\right) + C_1 \mu_t \frac{\varepsilon}{K}\frac{\partial v_j}{\partial x_i}\left(\frac{\partial v_i}{\partial x_j} + \frac{\partial v_j}{\partial x_i}\right) - C_2 \rho \frac{\varepsilon^2}{K} \qquad (7)$$

where $\partial/\partial x_i$ = differentiation with respect to coordinate direction x,y, or z (m)
K = turbulent kinetic energy field, m^2/s^2
ε = turbulent dissipation field, m^2/s^3
ρ = density (kg/m^3)
μ_t = turbulent viscosity (kg/m-s)
v_i = velocity component in x, y, or z direction (m/s)
σ_K, σ_ε = empirical constants (1.0, 1.3)
C_1, C_2 = empirical constants (1.44, 1.92)
i, j = coordinate direction indices; which when repeated in a term, implies the summation of all possible terms.

To model two phase flow when argon gas is injected, an additional set of momentum conservation equations was solved for the gas phase. Interphase coupling terms were added to account for the drag in proportion to the relative velocities of the liquid and bubble phases, which were generally in the Stokes or Allen regimes. The equations were solved using the CFX 4.2 finite difference package using half the standard reduction factor values for K, ε, and P, twice the standard number of sweeps, and deferred correction for K and ε for the first 500 iterations. The nozzle domain in Fig. 1 was divided into 74 blocks and discretized with 10,620 nodes and typically required 2.5 hours of computation on an Origin 2000 for 1000 iterations needed to converge to a steady-state solution unless the gas fraction was very large. The mold domain employed 6 blocks with 114,000 nodes and required about 10 hours of computation.

Boundary Conditions

The boundary conditions for the nozzle domain are included in Figure 1. The gas injection region, on the surface of the upper tundish nozzle (UTN) wall, is specified as a fixed velocity boundary for the gas phase. The fixed normal velocity for the gas phase is the gas injection flow rate through that region divided by the region area. It should be noted that the argon gas flow rate used in modeling is always the "hot" argon flow rate, which is about 5 times greater than the "cold" flow rate to account for thermal expansion.

Fixed pressure boundary conditions are specified at the outlet, or the ports of the nozzle. The specified pressure is set to the hydrostatic pressure (which depends on the SEN submergence depth), which is reasonably close to the actual pressure at the nozzle ports. Zero normal gradients are set for all transported variables (u, v, w, K, ε). This treatment of the outlet has proven to be an acceptable approximation for the conditions at the nozzle ports in previous works on single-phase flow [2, 3].

Figure 2 (b) shows the boundary conditions for the mold simulation. As a first step, the flow in the water model is assumed to be symmetric so only half is simulated to reduce computational resources. The inlet for the LES model is obtained by simulating the fully-developed turbulent flow in a square duct [8]. The flow from the exit of the duct is then directed at an angle of 30^o into the simulation inlet. The top surface assumes a rigid wall with a free-slip condition. The water level on the top surface was recorded with an ultrasonic flow sensor and averaged to determine its position for the model. Level fluctuations were about 3mm.

IV. Nozzle Results

Flow pattern observations

Flow patterns observed in the experiments can be directly compared to the numerical simulation with the model described above under the same operation conditions. In both the water experiments and model predictions, three main recirculation zones are observed inside the slide-gate nozzle: in the cavity of the middle gate plate, below the throttling gate plate, and at the nozzle ports. High gas concentration collects in these recirculation zones. Figure 3 shows an example of the predicted flow pattern near the nozzle ports. In both the simulation and the water experiments, the jet exits the ports with a single strong vortex or swirl. The vortex rotational direction is relatively stable with clockwise direction in a side view (y-z plane) at the plane of the port exit, looking directly into the left port (Figure 3A). The jet is directed approximately 29° down, as seen in the photograph of

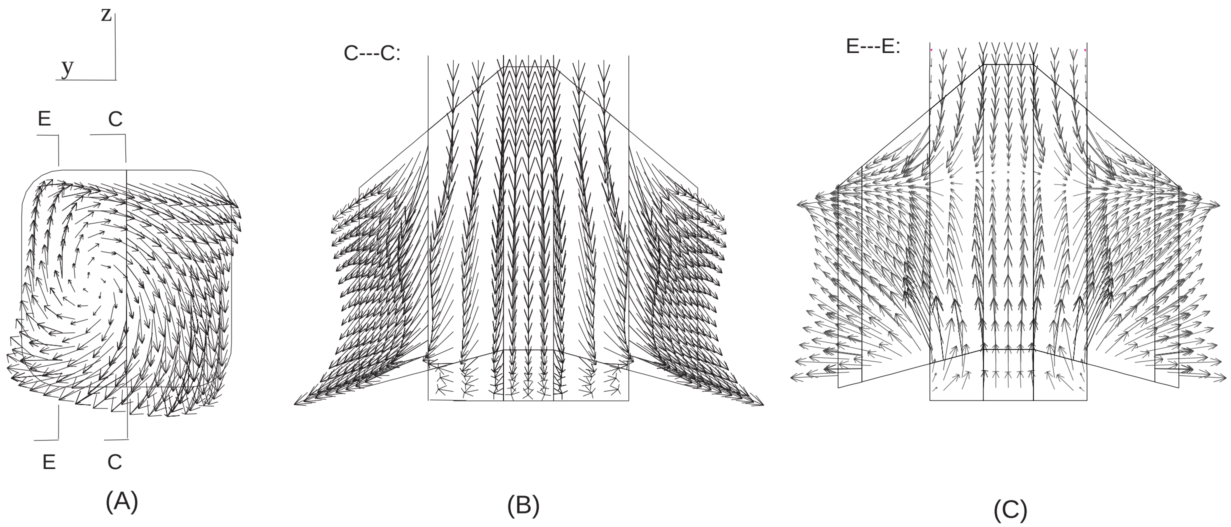

(A) (B) (C)

Figure 3 - Flow pattern predicted at the SEN ports for the experimental nozzle: (A) end view from the left port, (B) center-plane parallel to the wide face, (C) 12 mm from center-plane, parallel to the wide face

Figure 4. This is very close to the value of 27.8° down calculated from the simulation results using a weighted-average method over all nodes on the port plane [9].

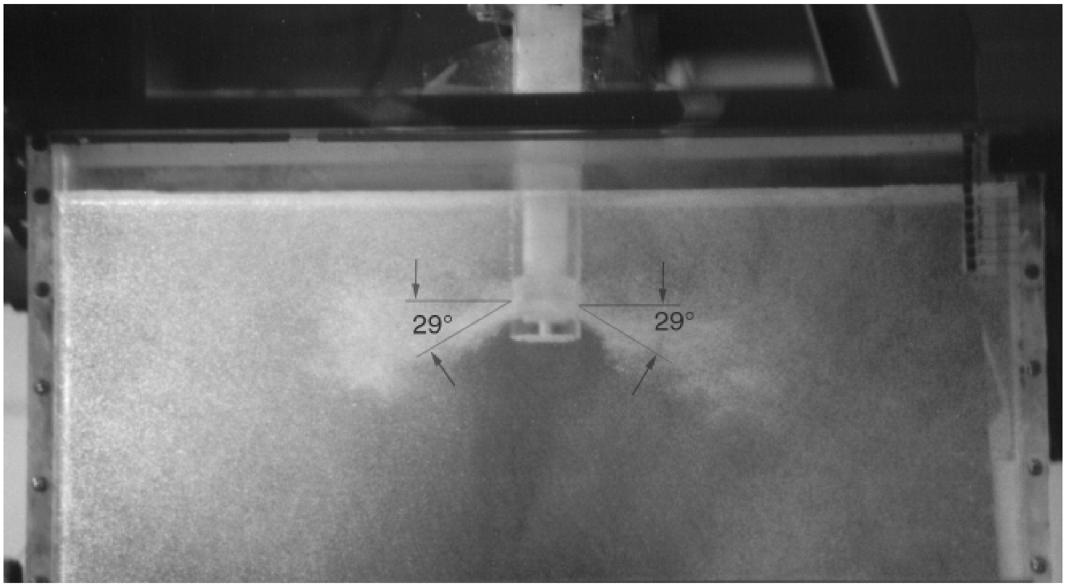

Figure 4 - Flow pattern and the average jet angle measurement in water model experiment

No obvious "back-flow" at the nozzle port was observed during the experiments. This matches the numerical computation, which predicts only outward flow at the nozzle ports, as shown in Figure 3. It is noted that the observation of no back-flow differs from many previous findings for typical nozzles [2, 3]. The zero back-flow-zone in the experiments is mainly due to the special design of the SEN ports of this nozzle, which had a much steeper angle of the upper port edges (40°down) than the lower port edges (15°down).

Velocity Comparisons

Quantitative comparisons between the PIV measurements and the simulation results were made on the jet at the nozzle port exit. An example is shown in Figure 5. Unfortunately, the flow field inside the plastic nozzle could not be reliably measured, due to the curvature of the nozzle wall and partial opacity from the machining cut. Figure 5(A) shows a vector plot of the PIV-measured flow field around the nozzle port in the plane parallel to the wide face of the mold. The predicted flow vector plots (B) are plotted side by side for direct visual comparison. The magnitudes of the liquid velocity at the port for measurements and prediction are then extracted and plotted together in (C). Since the PIV is a planar measurement which does not include v-component of the velocity (y-direction, perpendicular to the paper), the velocity magnitude is calculated using only the u- and w- velocity components. The "overall jet angle", defined as the weighted-average over the whole 3-D jet [3], should not be compared with the 2-D jet angle calculated from a single slice of the PIV measurements, or "slice jet angle". The slice jet angle is a simple arithmetic average of the jet angles for all measuring points (PIV) or computational cells (CFX) at the slice of the nozzle port. The time-averaged values of the "slice jet angle" are marked on Figure 5 (C).

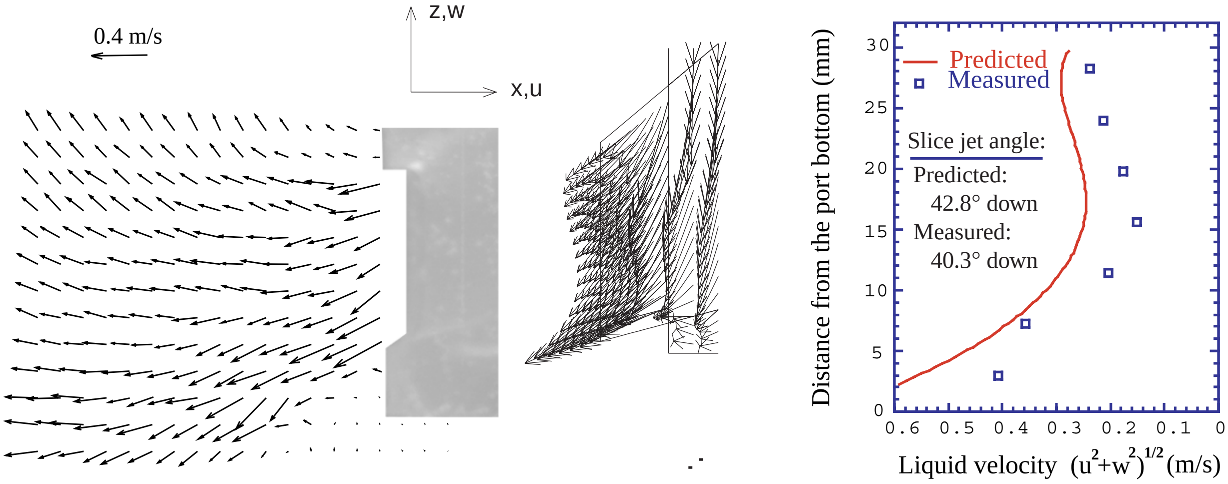

Slice (y=0) at the center-plane of the nozzle, parallel to the wide face of the mold

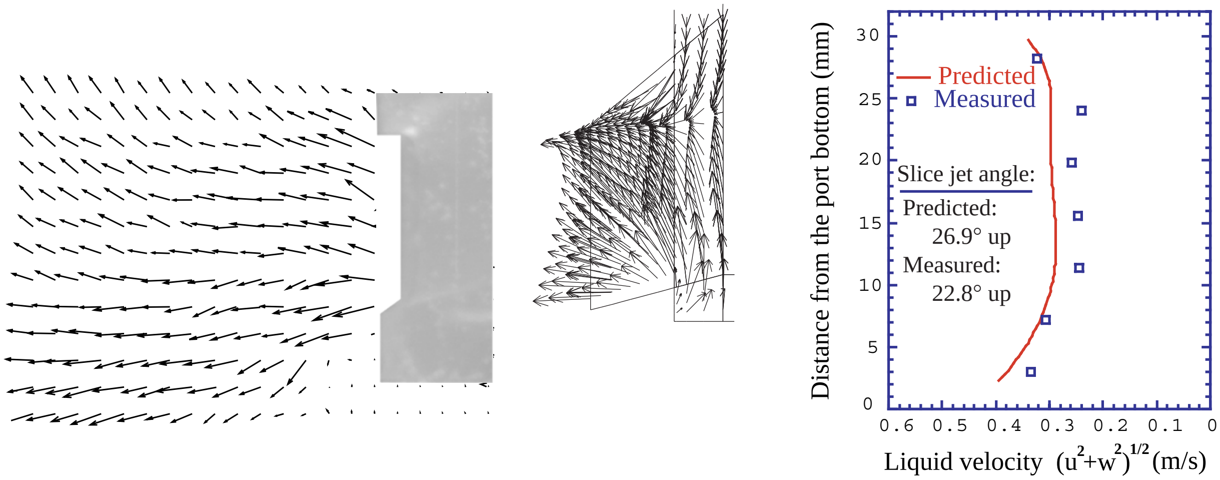

Slice (y=12mm) away from the center-plane of the nozzle, parallel to the wide face of the mold

(A) PIV measurements **(B) CFX prediction** **(C) Magnitute comparison of PIV measurements and CFX prediction**

Figure 5 – Comparison of PIV measurements and model prediction

The upper part of Figure 5 is for the slice through the nozzle center-plane (y=0), and the lower part for the slice that is away from and parallel to the center-plane (at y=12mm). The match of the velocity magnitude and the slice jet angle between the PIV measurement and the model prediction is satisfactory except that the velocity predictions are consistently slightly larger than the measurements. This is likely due to fact that the location of the pulsed laser light sheet was manually adjusted by naked eye during the PIV experiments, and thus might not lie exactly in the desired position. Figure 6 shows how the velocity magnitude might change with the slice location due to the 3-D effect of the jet vortex. It is interesting to notice the flow vector plot at the slice away from the center-plane (lower part of Figure 5). The jet in this slice is upward even though the overall jet is downward. This is consistent with the 3-D swirl of the jet discussed earlier.

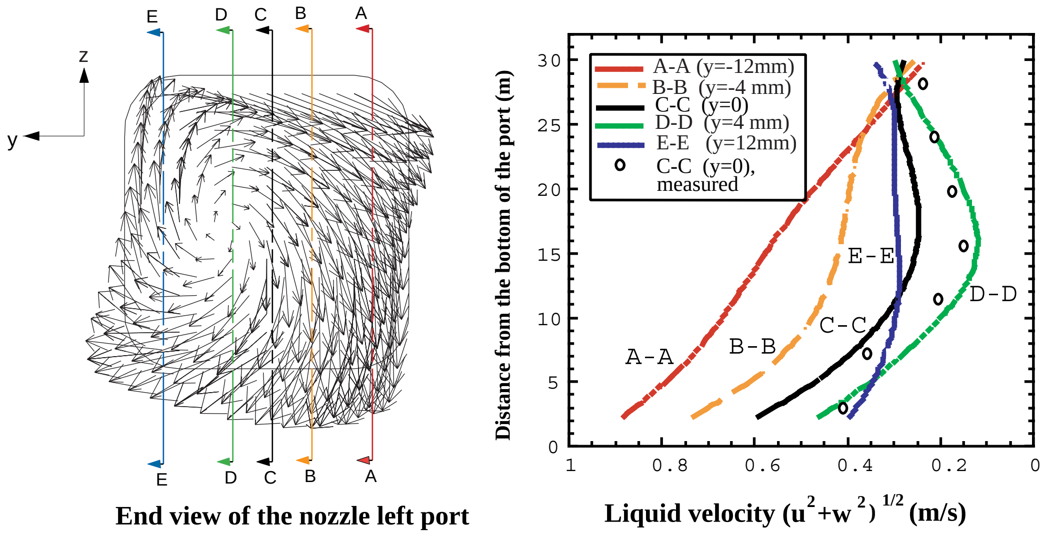

End view of the nozzle left port

Figure 6 – Velocity profile at different vertical slices of the nozzle port

V. Mold Region Results

Figure 7 shows a side to side comparison of a typical instantaneous vector plot along the center plane of the water model, parallel to the wide faces, obtained from the simulation (a) and PIV measurements (b). Figure 8 compares the corresponding time averaged vector plots. Each side of Figure 8 is made with an equal number of vectors in the X and Y directions. The simulation vector plot is time averaged over 60s.

The PIV vector plot is a composite containing three time-averaged parts. The three parts are the top region containing the upper roll and the jet which has been averaged over 10s (50 snapshots), the middle region containing lower roll (0.25-0.65m below water surface) averaged over 200s (200 snapshots), and the bottom region extending from 0.65m - 0.77m averaged over 40s (200 snapshots). The middle region is also a spatial average of the right and left half regions of the water model, in order to average the considerable differences which arose due to asymmetry between sides. The maximum number of vectors in a region was reduced 8-fold to 568 in order to maintain good resolution, with 31 along the horizontal and 19 along the vertical in accordance with the camera aperture.

In both the simulation and the experiment, the jet emerges at an angle of approximately 30^o downward. It bends slightly as it traverses the mold to impinge on the narrow face. The flow then splits upward and downward. Due to the high velocity of the jet, a low-pressure region is created in and around the jet resulting in the entrainment of fluid from both above and below. This helps to form the "upper" and "lower" recirculation regions above and below the jet.

The simulation and PIV measurements generally compare very well, both qualitatively and quantitatively. This includes the angle and shape of the jet, upper and lower rolls. Both the measured and simulated velocities in the region near a diagonal from the top-left corner to the center of the upper roll are lower than the velocities up the narrow face and across the water surface.

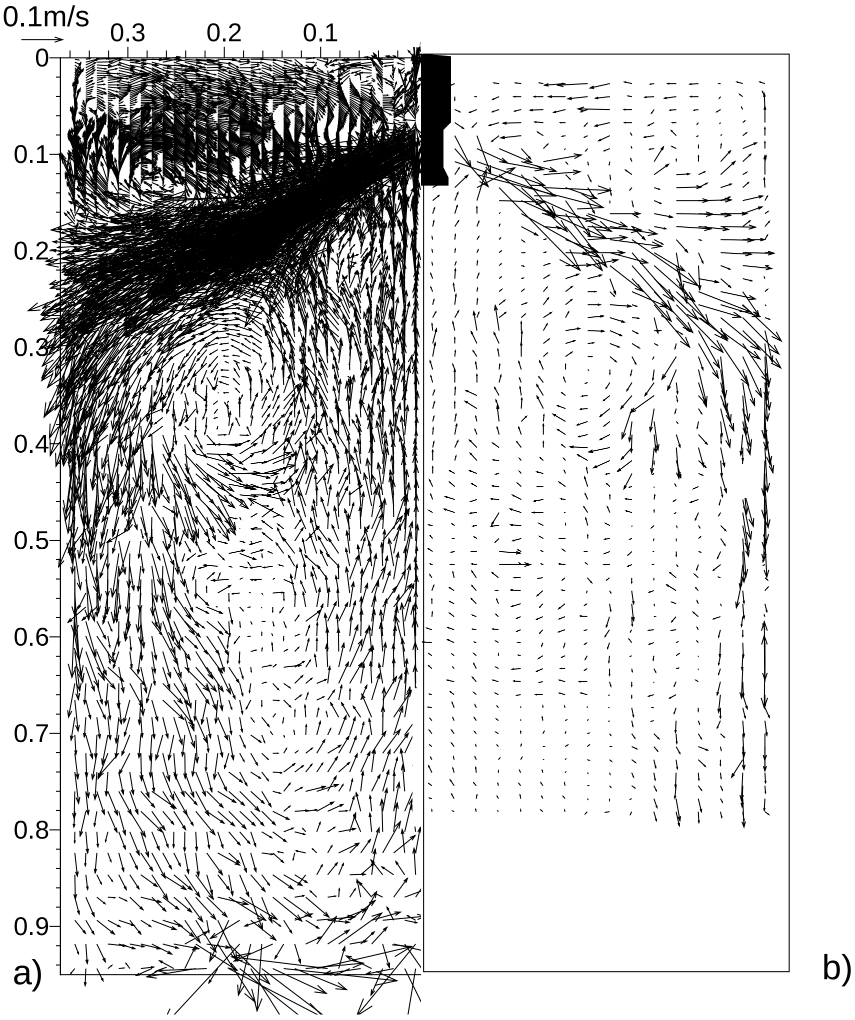

Figure 7: Instantaneous velocity vector plot of (a) simulation and (b) PIV measurement

Figure 8 (c) shows velocity vectors in a plane 20 mm from the narrow face which explains the reason for these low velocities in the corner. As seen in the figure, the jet impinges on the narrow face and spreads in all directions.

Flow is then stronger up the corners than in the center plane parallel to the wide face. This split flow rejoins close to the top surface, some distance from the narrow face. This is responsible for the apparent region of low flow mentioned above.

The PIV jet appears to bend slightly more than the simulation jet as it moves towards the narrow face. The biggest discrepancy, however, is that the upward-moving velocities in the region directly below the SEN in the experiment are smaller than in the simulation.

Figure 9 is a sample plot of time variation of velocity at a point close to the top surface, halfway between the SEN and the narrow face. The PIV points are spaced 0.2s apart as compared to 0.001s increments in the simulation. The PIV velocity variation shows the existence of two time scales. The short time scale is about 0.7s and is predicted well by the simulation.

The longer time scale is at least 45s. It results in times of 5s or more when the velocity close to the top surface is three to four times the mean. This period of high velocity could shear the molten flux layer and cause its entrainment deep into the caster. These long time-scale variations caused by the wide variations in the depth of penetration of the experimental jet are not seen in the simulation.

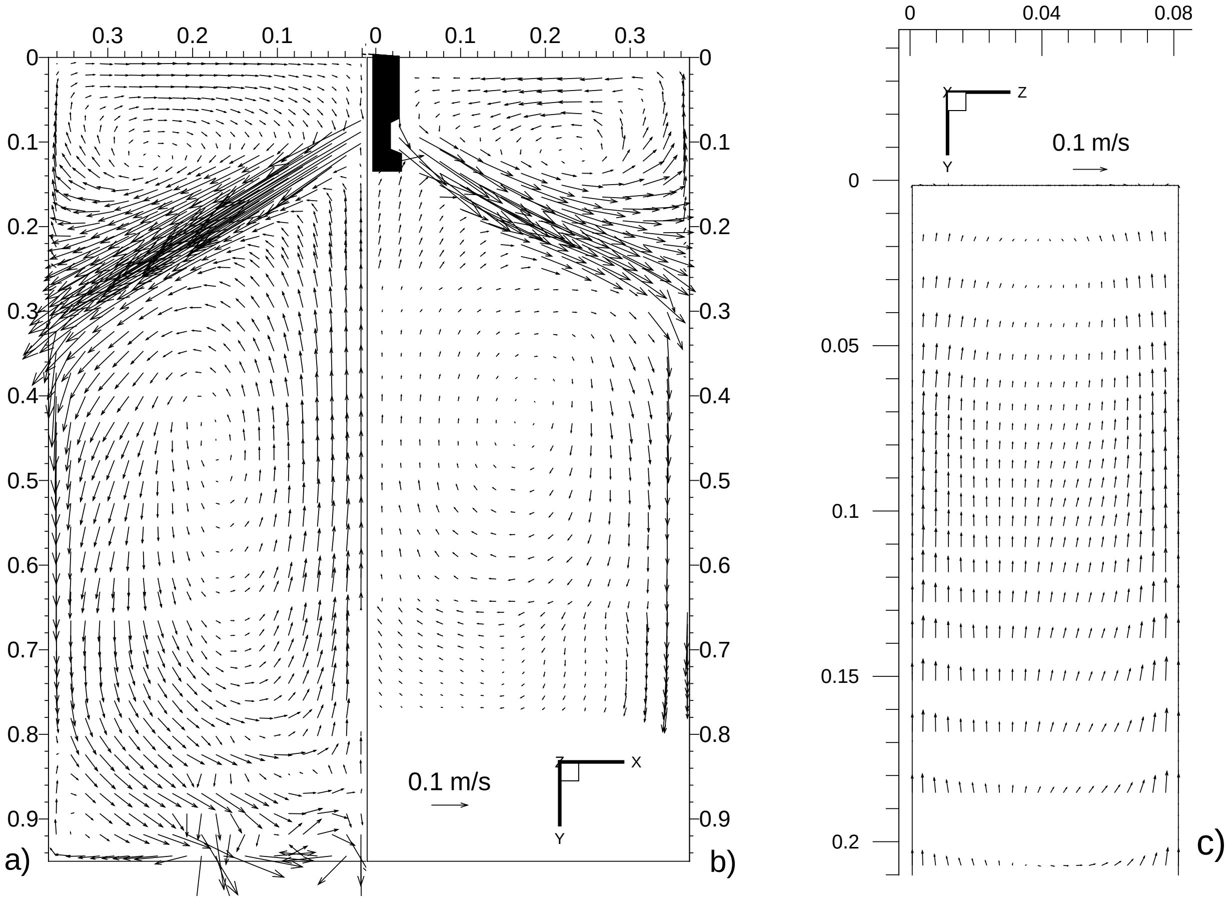

Figure 8: Time averaged velocity vector plot of (a) simulation and (b) PIV; (c) Time averaged velocity vectors from the simulation parallel to and 20mm from the narrow face.

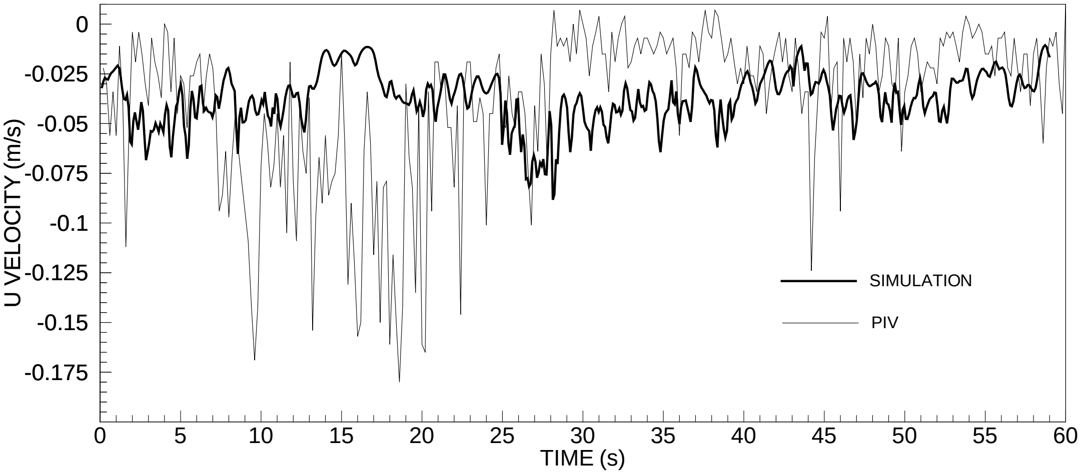

Figure 9: Typical history of U velocity component below the water surface in simulation and PIV.

Figure 10 (a) shows a schematic of the flow from the port that illustrates the swirling jet. The perpendicular movement of the slide gate flow control positioned high in the nozzle tube, (relative to the wide face) allows flow through only 41% of the nozzle bore area. This causes stronger flow down the inner radius wide face side of the nozzle. This bias in flow over the cross section continues causes the experimental jet to swirl as it exits the nozzle ports. This persists into the mold cavity, where the jet centerline moves along a helix, as depicted in the figure. The overall jet moves downward at an angle of 30^o and the swirl gradually diffuses.

The swirling experimental jet moves both up-down and in-out of the center plane. As a result of the helical motion, strong regions of the flow have either an upward or downward component, depending on the radial location. The in-out motion of the jet results in this vertical component of flow to often occur in the center plane in the PIV measurements. This results in a net instantaneous jet of angle significantly greater than 30^o. Also because of the helix, alternate regions of the flow have an angle less than 30^o. This results in a staircase type of pattern as seen in Figure 10 (b).

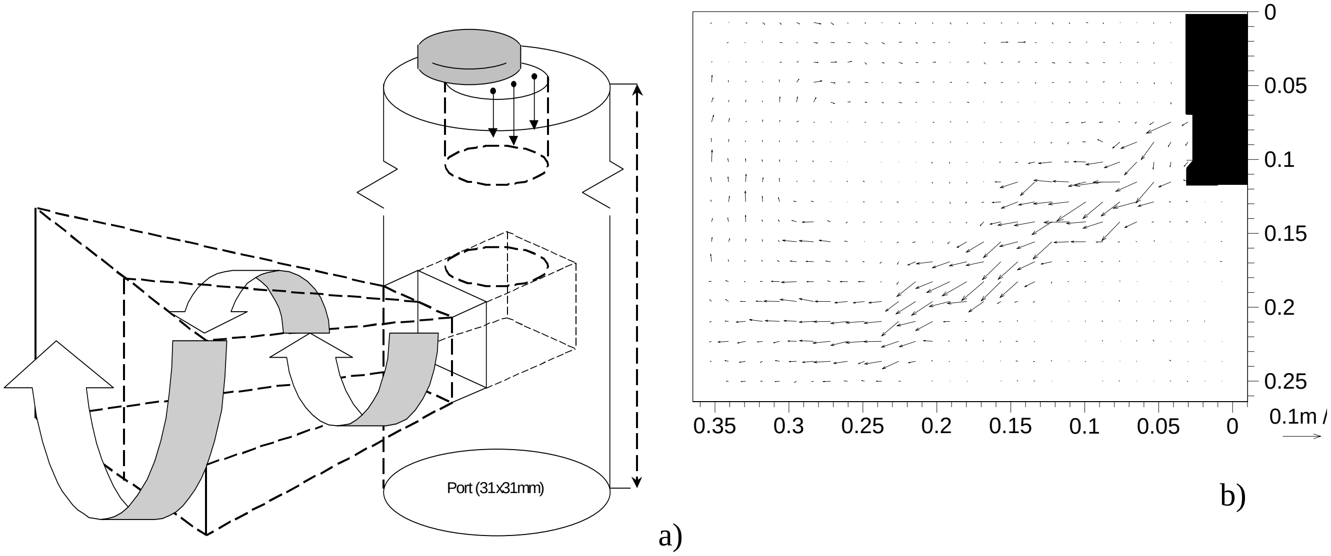

a)

b)

Figure 10: (a) Schematic of swirling flow in the PIV jet; (b) The in-out of plane motion of this swirl results in distinct staircase pattern in a instantaneous PIV vector plot of the center plane.

As the jet moves in and out of the center plane at a given point, either the upward or downward moving portion of the spiral flow will be present. This causes the staircase shape to alternate. The time scale of this alternation, and corresponding in-out of plane motion is of the order of 0.2s. In addition the entire jet chaotically alternates between shallow and deep penetration. The jet also has an in-out motion on a large time scale, resulting in the frequent intermittent disappearance of vectors close to the narrow face, for periods of about 7s. The simulation jet also has miniature staircase patterns which result from jet wobble due solely to turbulence, which is consistent with previous work [10]. However the deviation from 30^o is much smaller than the PIV measurement and the different staircases are out of phase.

This finding implies that the inlet swirl persists more than halfway across the mold. This may significantly affect the flow features in other regions of the mold and explain some of the discrepancies in the results. Thus it is necessary to incorporate the swirling inlet condition along with the in-out of plane motion in future simulations.

The speed predicted along the axis of the jet by both the LES and CFX models is compared in Figure 11 with the PIV measurements. The K-ε model treats the swirl at the inlet by imposing the velocities, K and ε values calculated by the nozzle model. This is seen to slightly over-predict the diffusion, leading to slower jet velocities than measured. The LES jet is slightly faster than the PIV measurements, due to the lack of swirl as already discussed.

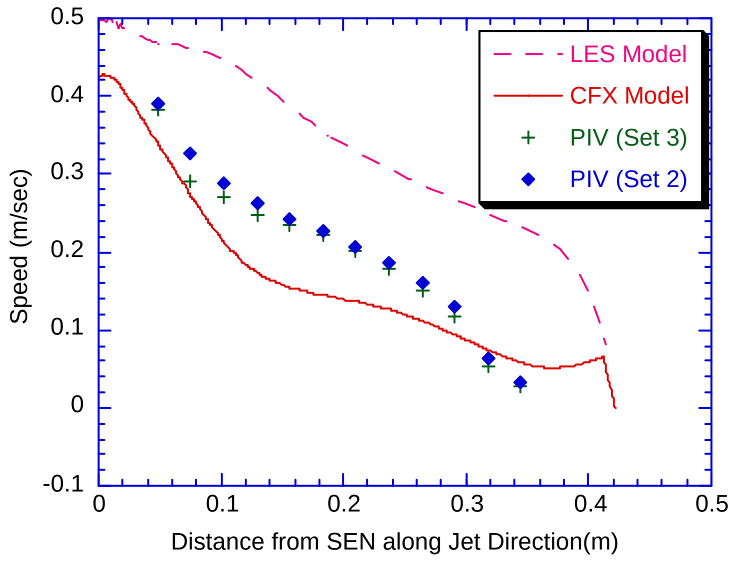

Figure 11 Comparison of LES, CFX, and PIV measured velocities (along jet centerline)

Figure 12 is an instantaneous vector plot of the velocities in the top region of the simulation. The upper roll at this instant is seen as a set of distinct vortex structures as opposed to the single large recirculation structure seen in the time average vector plot (Figure 8(a)). The top region alternates chaotically between these two extremes.

Figure 13 is a 30-min time averaged vector plot of the velocities measured in the lower rolls of the water model. Considerable asymmetry can be seen between the left and right rolls, which persist even over this long time period.

There are two main features of this asymmetry that are especially significant. One is the region of very low velocity below the impingement point on the right, which contrasts with the higher downward flow on the left. This asymmetry was likely caused by an angular misalignment of the nozzle of the order of 1^o in the X-Z plane resulting in the jet on the right moving out of the center plane. Dye injection study for the same configuration, without change in the flow settings is consistent with this angular misalignment. The second is the upward moving flow below the SEN being directed towards the left. This suggests a period of time when the right roll is larger than the left. Study of the transient flow features over this 30-min. period reveals a repeating sequence of three features when: 1) Both rolls are about the same size for about 17s; 2) Right roll is larger than the left for about 30s and 3) A short-circuited structure forms and merges into lower roll over about 14s, while both rolls are about the same size.

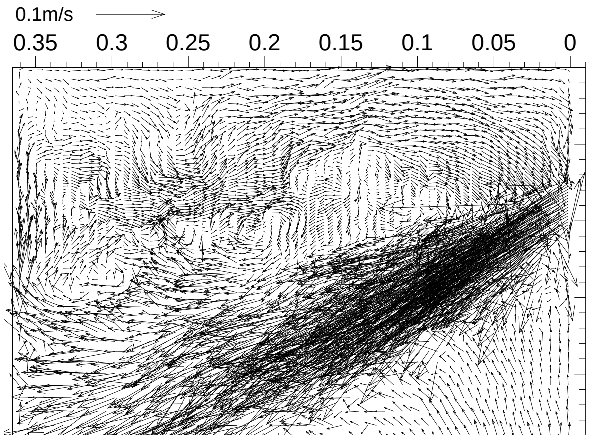

Figure 12: Instantaneous vector plot of the velocities in the top region of the simulation.

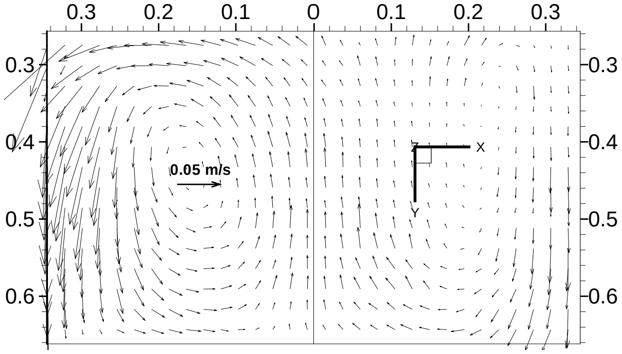

Figure 13: 30 min (2000 snapshots) time averaged vector plot of the velocities in both the lower rolls.

The simulation enforces symmetry by simulating only half of the domain with a symmetry boundary condition. The presence of this significant asymmetry necessitates the simulation of both halves of the water model / caster in future work. Figures 7 (a) and (b) show an instant when the short circuit between the upward and downward flows of the lower roll has taken place and the downward motion of the location of the short circuit has begun. The short-circuit of the downward moving flow of the lower roll with the upward moving portion is seen in both experiment and simulation. This suggests that it is an inevitable consequence of pressure instabilities or other natural disturbances in the flow field, which are not caused solely by the inlet conditions. This phenomenon is important for particle or bubble entrapment and needs to be investigated further.

VI. Conclusions

The turbulent flow of liquid steel and argon bubbles in a slide-gate nozzle and mold can be simulated with three-dimensional finite difference models. Model predictions agree both qualitatively and quantitatively with the measurements conducted using PIV (Particle Image Velocimetry) on a 0.4-scale water model in this paper. Together, the PIV measurements and simulation reveal deeper insight into of flow in the continuous casting process, in particular regarding transient phenomena.

The inlet condition is very significant to the flow in the mold. Strong swirl is generated at the port outlet by the 90˚ oriented slide gate nozzle. This causes considerable in and out of plane motion, which persists at least halfway across the mold. This was not captured in the LES simulation, which has a simple inclined fully-developed turbulent square duct flow as its inlet condition.

Flow across the top surface in the physical model varies by more than 100% of its mean value. This variation includes a high frequency variation (~1.5 Hz) which is also seen in the simulation. It also includes of a low frequency component (time period of the order of 45s) which results in durations of 5s or more when the horizontal velocities are 3-4 times larger than their mean values. This component is not seen in the simulation and might be due to variations stemming from fluctuations in the inlet conditions. This feature is likely significant to shear entrainment of the liquid flux.

Although the entire geometry including the inlet nozzle and its port were symmetric, there was considerable, persistent, asymmetry between the two lower rolls. Flow in this region alternates through a sequence of flow phenomena, which repeats chaotically. One of the flow features involving short circuiting is seen in both the physical model and the simulation, suggesting that it is inherent to the turbulence and not caused solely by the inlet conditions. This feature is important for particle motion and bubble entrapment, which are responsible for defects in the final product.

VII. Acknowledgements

The authors would like to thank the National Science Foundation (NSF - Grant # DMI - 98-00274) and the Continuous Casting Consortium (CCC) at the University of Illinois at Urbana Champaign (UIUC) for their support of this research, the National Center for Supercomputing Applications (NCSA) at the UIUC for computing time, AEA technology for use of the CFX4.2 package, Tiebiao Shi for the CFX mold simulation figure, and especially Dr. Mohammed Assar, Dr Pierre Dauby and the technicians at LTV Steel for their help with the PIV measurements.

VIII. References

1. L.M. Mika, B.G. Thomas and F. Najjar, "Simulation of Fluid Flow Inside a Continuous Slab Casting Machine," Metallurgical Transactions B, 21B (1990), 387-400.
2. D.E. Hershey, B.G. Thomas and F.M. Najjar, "Turbulent Flow through Bifurcated Nozzles," International Journal for Numerical Methods in Fluids, 17 (1993), 23-47.
3. F.M. Najjar, B.G. Thomas and D.E. Hershey, "Turbulent Flow Simulations in Bifurcated Nozzles: Effects of Design and Casting Operation," Metallurgical Transactions B, 26B (4) (1995), 749-765.
4. D. Xu, W.K. Jones and J.W. Evans, "PIV Physical Modeling of Fluid Flow in the Mold of Continuous Casting of Steel," in Processing of Metals and Advanced Materials: Modeling, Deisgn and Properties, B.Q. Li, eds., (TMS, Warrendale, PA, 1998), 3-14.
5. S. Sivaramakrishnan, H. Bai, B.G. Thomas, P. Vanka, P. Dauby, M. Assar, "Transient Flow Structures in Continuous Cast Steel" (Paper to be presented at Steelmaking Conference, Pittsburgh, PA, March 26-29, 2000, ISS, Warrendale, PA), 83.
6. H. Bai and B.G. Thomas, "Two-phase flow in tundish nozzles during continuous casting of steel slabs" (Paper to be presented at Materials Processing in the Computer Age III, Nashville, TN, March 12-16, 2000, TMS, Warrendale, PA).
7. J. Tannehill, D. Anderson and R. Pletcher, Computational Fluid Dynamics and Heat Transfer, (Washington, DC: Taylor and Francis, 1997).
8. R. Madabushi and S.P. Vanka, "Large Eddy Simulation of Turbulence-Driven Secondary Flow in a Square Duct," Physics of Fluids, 3 (11) (1991), 2734-2475.
9. B.G. Thomas, "Mathematical Models of Continuous Casting of Steel Slabs" (Report No. 1998, Continuous Casting Consortium, University of Illinois at Urbana-Champaign, 1998).
10. R.V. Wilson and A.O. Demuren, "Numerical simulation of turbulent jets with rectangular cross section," ASME J of Fluids Eng, 120 (Jun) (1998), 285-290.